Volume 17
Number 28
28 July 2021
Pages 6679–6902

Soft Matter

rsc.li/soft-matter-journal

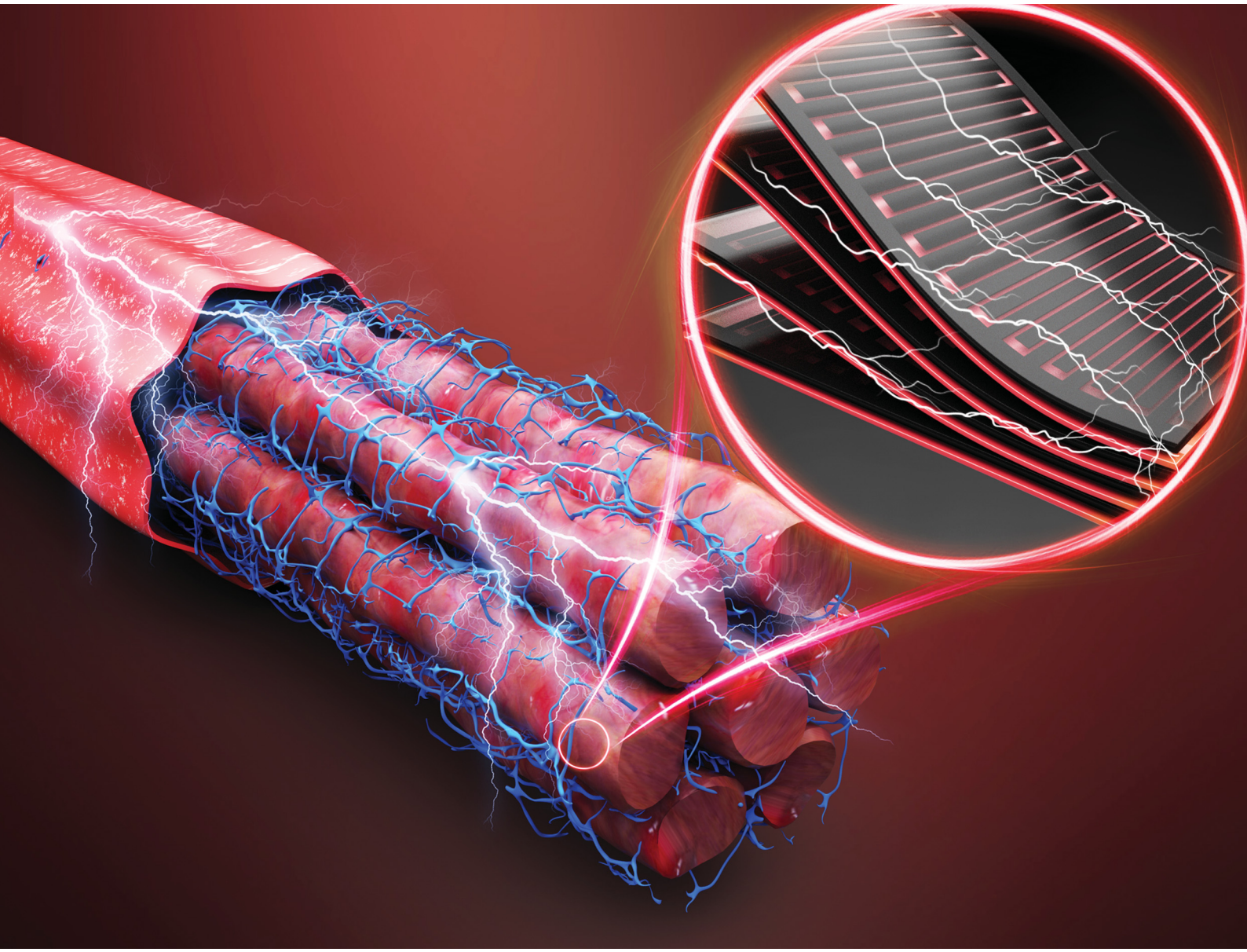

ISSN 1744-6848

ROYAL SOCIETY OF CHEMISTRY

PAPER

Bo Li, Ketao Zhang, Hualing Chen *et al.*
3D printable and fringe electric field adhesion enabled variable stiffness artificial muscles for semi-active vibration attenuation

Soft Matter

PAPER

View Article Online
View Journal | View Issue

Check for updates

Cite this: *Soft Matter*, 2021, 17, 6697

3D printable and fringe electric field adhesion enabled variable stiffness artificial muscles for semi-active vibration attenuation†

Chen Liu, ‡[a] Bo Li,‡*[b] Zhuoyuan Li,[b] Chongjing Cao,[c] Xing Gao,[c] Ketao Zhang*[a] and Hualing Chen*[b]

Received 26th April 2021,
Accepted 26th May 2021

DOI: 10.1039/d1sm00618e

rsc.li/soft-matter-journal

Soft robots are able to generate large and compliant deformation in an unconstructed environment, but their operation capability is limited by low stiffness. Thus, developing the function of variable stiffness while preserving its compliance is a challenging issue. This study proposes a new variable stiffness artificial muscle, as a complementary component for soft robots, using the principle of fringe electric field adhesion. Taking inspiration from the mechanism of multi-layer structures in biological muscles, the artificial muscle is composed of patterned conductive layers and interlayers and is 3D printable by direct ink writing (DIW). To further demonstrate the application, a vibration absorber by stacking this artificial muscle is proposed, whose natural frequency is tunable by the varying stiffness. The advantages of the fringe electric field-enabled variable stiffness (FEVS) artificial muscles include lightweight and irrelevance of the stiffness to the thickness of the interlayer, which can be beneficial to soft robots to achieve variable stiffness and semi-active vibration attenuation without extra weighting load.

Published on 27 May 2021. Downloaded on 7/22/2021 12:35:26 PM.

1. Introduction

Soft robots have an inherent softness that entails higher degrees of flexibility and adaptability to the environment compared to rigid-bodied robots. To further advance soft robotics, it necessitates the new development of soft actuators for soft robots. By integrating soft functional materials, *i.e.*, electroactive polymers[1] or gels,[2] these actuators are capable of large deformation.[3,4] There are several types of soft actuators, which can be classified by the physical principle as pneumatic actuators,[5,6] electrical actuators,[7] hybrid bio-material actuators,[8] optical actuators,[9,10] *etc.* Consequently, the so-developed soft robots have been demonstrated with capabilities of biomimetic motions, *i.e.* crawling, swimming, and flying.[11–15] Through the success of design and analysis, the soft robot is able to be engineered to execute operations by partly replacing conventional rigid-bodied robots.[16]

Meanwhile, their applications are limited due to the softness when high force transmission is needed. Low stiffness in the soft material limits performance of soft grippers in certain operations.[17,18] For instance, soft robots have been adopted in medical applications such as in invasive surgery, but their lack of high stiffness fails to provide mechanical support for further operation. Thus, developing new soft robots encompassing both flexibility and variable stiffness is an urgent need.[14,15,19–21]

The realization of variable stiffness in soft actuators has been achieved using different strategies.[10,22–26] For instance, the pneumatic variable stiffness structures can achieve a significant stiffness change by generating vacuum and enabling jamming between the particles.[27–30] However, it often requires a bulky vacuum pump that is affiliated with the robotic system.[31–33] The thermally driven shape-memory materials and low melting point alloy are able to tune the stiffness over a large span in elastic modulus but fail for fast and real-time adjustment.[34–38] On the other hand, electrically driven variable stiffness in a soft actuator has become a favourable method for fast and wire-connected regulation.[39–41] Subject to an electroadhesion (EA) force, the thin polymer films, coated with compliant electrodes, are compressed to form a condensed unit block, which consequently alters the structural stiffness.[42–45] Due to the advantage of fast actuation, the electrical field-based variable stiffness method has been developed,[46–50] among which the fringe electric field has a unique feature of being less dependent on the material and thickness of the adsorbed object when compared with electro-bonding laminates.[51–54] In previous studies, this type of adhesion was mostly used in robot motion including soft grippers and wall-climbing but a

[a] *Centre for Advanced Robotics (ARQ), Queen Mary University of London, London E1 4NS, UK. E-mail: ketao.zhang@qmul.ac.uk*
[b] *State Key Lab of Manufacturing Systems Engineering, Shaanxi Key Lab of Intelligent Robots, School of Mechanical Engineering, Xi'an Jiaotong University, Xi'an 710049, P. R. China. E-mail: liboxjtu@xjtu.edu.cn, hlchen@xjtu.edu.cn*
[c] *Research Centre for Medical Robotics and Minimally Invasive Surgical Devices, Shenzhen Institutes of Advanced Technology (SIAT), Chinese Academy of Sciences, Shenzhen 518055, P. R. China*

† Electronic supplementary information (ESI) available. See DOI: 10.1039/d1sm00618e
‡ C. L. and B. L. contributed equally.

Published on 27 May 2021. Downloaded on 7/22/2021 12:35:26 PM.

variable stiffness performance based on such EA has not yet been reported.[55–58]

Based on the principles of fringe electric field and biological inspiration, this study designs a variable stiffness artificial muscle using EA technology by fringe electric field on layered artificial muscles. This artificial muscle is fabricated by a 3D printing technique and its stiffness tuning performance is characterized in-depth. To further demonstrate the variable stiffness capability, a vibration absorber, by stacking layers of artificial muscle unit, is designed and tested, where a change of its natural frequency is realized as a strategy of semi-active control. Finally, a discussion comparing the variable stiffness behaviors is conducted following by a conclusion.

2. Preparation and characterization

2.1 Design principle and 3D printing of FEVS

The working principle of the proposed variable stiffness of the artificial muscle is inspired by the contraction and stiffening of muscle fibre, as Fig. 1(a) shows.[59,60] A muscle is composed of a large number of fibre bundles. The fibre bundles can be divided into multiple myofibrils, which are mainly the thick and thin filaments. When the muscle contracts, thick and thin filaments become close and compress each other, leading to an increase in the overall stiffness in the muscle. Inspired by this mechanism, this study proposes a design of an artificial muscle utilizing the principle of EA by a fringe electric field.

As sketched in Fig. 1(b), the fringe electric field-enabled variable stiffness (FEVS) artificial muscle is a laminated multiple layer structure with alternately stacked EA pads and interlayers. The function of the EA is realized by the fringe electric field, which is generated by the alternatively laid out positive/negative electrodes in the EA pad. When a voltage is applied, a fringe electric field polarizes the surface of the interlayer and introduces charges that are distributed in an orderly manner.[61] As a result, a new electric field is generated between the EA pad and the interlayer, producing an attraction force within. Similar to the muscle becomes rigid, the EA pads could be considered as thick

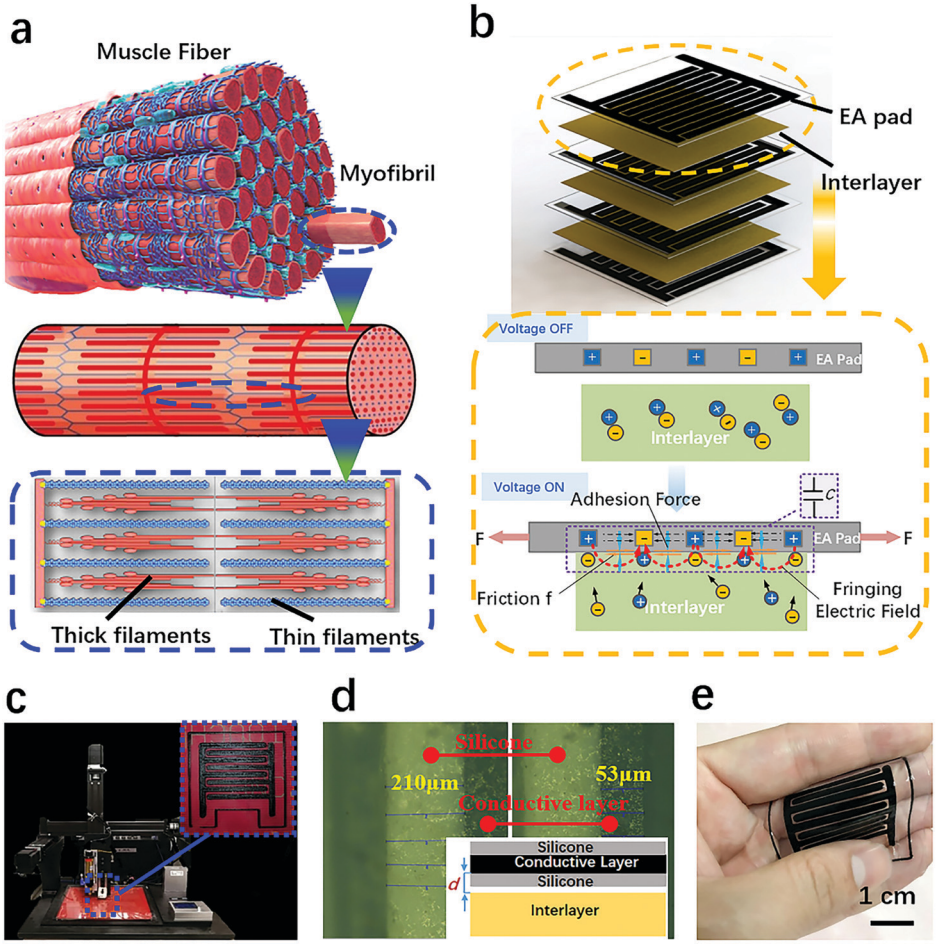

Fig. 1 Design and 3D printed FEVS artificial muscle. (a) The constitution of biological muscle. When muscle contracts, the thick and thin filaments approach and compress each other so that the overall stiffness increases. (b) Schematic of the proposed FEVS artificial muscle with alternatively sandwiched EA pads and interlayers. The material of the interlayer is tinfoil with a rough surface. When the voltage is off, there is no attraction between the EA pad and the interlayer. When the voltage is on, the EA pad and the interlayer attract each other. Under the adhesion, a friction f is induced in the artificial muscle, which increases the stiffness of the whole structure. (c) The DIW 3D printer and a printed EA pad with comb patterned electrodes. (d) Thicknesses of the silicone layer (white part) and the conductive electrode layer (dark part). (e) Illustrating the flexibility of the EA pad.

 This journal is © The Royal Society of Chemistry 2021

Published on 27 May 2021. Downloaded on 7/22/2021 12:35:26 PM.

filaments and the interlayers are thin filaments. Under the electrostatic forces, the EA pads and the interlayers attract and compress each other, like thick and thin filaments, thus increasing the pressure and friction between them to finally improve the overall stiffness of the structure. Unlike the conventional electro-laminates, where the electric field has to penetrate through the interlayer, the fringe electric field acts only on the surface of the interlayer, regardless of its thickness level while it offers an even higher electric field.

The EA pad with comb patterned electrode was fabricated by 3D printing in the direct-written method (Fig. 1(c)). Fig. 1(d) displays the cross-section of the EA pad, with silicone layers and conductive layers. The thickness of the conductive layer is 53 μm and the silicone rubber layer is about 210 μm, which are consistent with the prescribed printing parameters. The fabricated EA pad has the size of 40 mm × 40 mm and can deform with the human hand which meets the requirements of full flexibility to resemble a piece of muscle, as shown in Fig. 1(e).

The principle of variable stiffness suggests that a better variable stiffness effect can be ensured when the friction between the EA pads and the interlayer is great. The shear force depends on two aspects: the normal attraction force and the contact surface roughness. The normal attraction force is closely related to the structural parameters of the electrode layer. It can be observed from Fig. 1(d) and 2(a) that the structural design parameters are: the electrode width a, the electrode effective area A, the gap d between the electrode layer and the surface of the absorbed object, and the gap d_1 between electrodes. The electrostatic attraction force F can be estimated as eqn (1), according to the existing literature.[57,58]

$$F = \frac{\varepsilon_r \varepsilon_0 a l}{2d^2} U^2 + \frac{0.265 \varepsilon_r \varepsilon_0 a^{0.5} l}{{d_1}^{1.5}} U^2 \quad (1)$$

where l is the electrode length. A is the effective area of the electrode, which is equal to $a \times l$. ε_0 is the vacuum dielectric constant. U is the applied voltage value. The relative permittivity between the electrode and the surface of the interlayer can be expressed as

$$\varepsilon_r = n_1 \varepsilon_{r1} + n_2 \varepsilon_{r2} + n_3 \varepsilon_{r3} \quad (2)$$

where ε_{r1} is the relative permittivity of the electrode encapsulation layer. ε_{r2} is the relative permittivity of air. ε_{r3} is the relative permittivity of the surface of the absorbed object, and n_1, n_2, and n_3 are the corresponding coefficients.

Eqn (1) suggests that the parameters which affect the output of attraction force are: d, d_1, a and l. In this work, the thickness of the silicone is maintained at 210 μm due to the restriction of the 3D printing resolution. The length l of the electrode is determined by the overall structural size of the electrode layer. As for the electrode spacing d_1 and electrode width a, due to the limitation of the test conditions, d_1 cannot be reduced indefinitely. Therefore, d_1 and a are the two key parameters that should be studied and optimized.

2.2 Characterization of FEVS

The printed FEVS is illustrated in Fig. 2(a). To study the relation between electrostatic attraction force and electrode comb width a and comb gap d_1, the following electrode size (electrode width/mm–electrode comb gap/mm) was set in the experiment: 2–1, 2–1.5, 2–2, 2.5–1, 2.5–1.5, 2.5–2, 3–1, 3–1.5, 3–2, 4–1, 4–1.5, and 4–2 (as numbered in Fig. 2(a)). Fig. 2(b) shows the measurement of the normal attraction force of the printed electrostatic layer, which is described in the materials and method section. In the study, tin foil was selected as the attracted objects since the metal materials have sufficient free electrons for a greater electrostatic force. The measured attraction force is divided by the effective area A to obtain the attraction stress

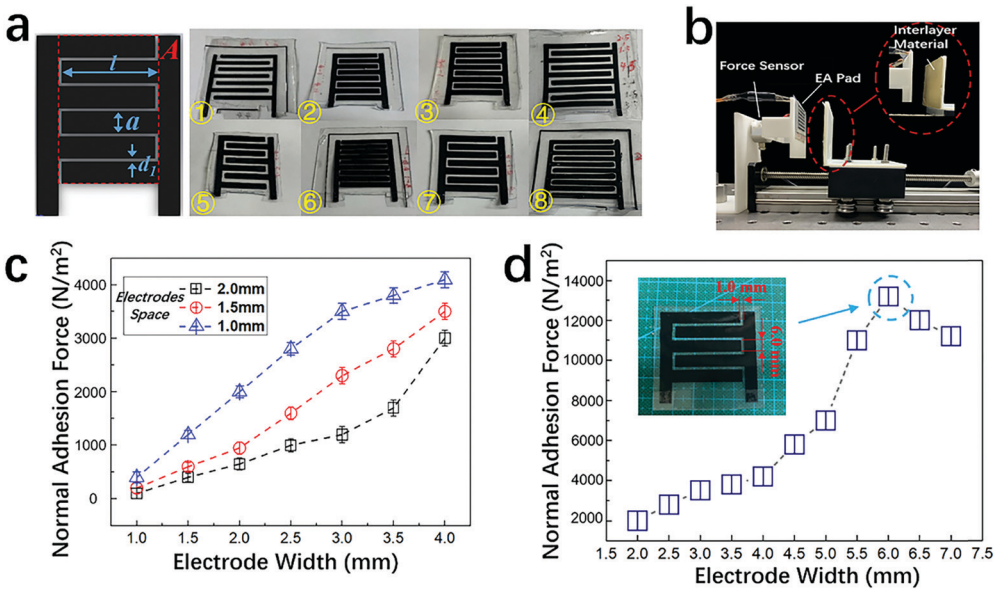

Fig. 2 The normal force of EA pads. (a) The EA pad design and the fabricated samples with different parameters. (b) The experimental setup for measuring normal attraction force. (c) The results of the EA pad's normal force at 3 kV. The EA pads had different sizes of electrode width and gap. (d) The result of normal forces of EA pads with different electrode widths with a 1 mm electrode gap. The pad with 6 mm electrode width has the best performance.

Published on 27 May 2021. Downloaded on 7/22/2021 12:35:26 PM.

(force per unit effective area), and the performance of the attraction with different structural parameters can be evaluated. In Fig. 2(c), the electrostatic attraction force at 3 kV increases with the width of the comb a, and a narrower the comb gap d_1 leads to a higher attraction force, which is consistent with the situation described in eqn (1). However, the comb gap cannot be reduced infinitely due to (1) the 3D printing resolution limitation and (2) the breakdown risk in the electrode. The minimum allowable comb gap was then limited to 1 mm. Therefore, we optimized the comb width dimension hereby. It was measured that the comb width increased from 2 mm with an increment of 1 mm until the attraction force began to decrease. According to the experimental results, when the comb width was 6 mm, the attraction force maximized locally was 135 000 N m^{-2}, as shown in Fig. 2(d). The reason for the inflection point occurring is when the comb width was beyond 6 mm, the comb width was too wide at this time, which reduced the number of electrode combs in a certain area (40 mm × 40 mm), then it would weaken the increase of the attraction force. Therefore, the comb width was prescribed as 6 mm in the study that followed.

After determining the electrode layer parameters, we proceeded to optimize the material of the interlayer. The working principle of this variable stiffness structure is to polarize the interlayer through the EA pad and to increase the interfacial friction. Therefore, to obtain a better effect of variable stiffness, the interlayer should meet the requirements of low friction before polarization and high friction after. Measurement of the shear force was illustrated in Fig. 3(a). In the experiment, the normal attraction force was measured on four materials as the interlayer (the size was 20 mm × 20 mm) including polyester film, printing paper, tin foil and cotton cloth. As shown in Fig. 3(b), when the voltage changed from 0 kV to 3 kV, the attraction force of the four materials increased by 2.1 N, 0.9 N, 2.9 N and 0.8 N respectively. Therefore, the attraction force of the tin foil changed most significantly. Apart from the influence of the material, the PET film and the tinfoil have relatively flat surfaces compared to the printing paper and the cotton, which will ensure that the EA pads have a larger true contact area, resulting in a greater adhesion force.[62]

In Fig. 3(c), the tin foils with different surface roughness (1200 mesh, 800 mesh, 400 mesh and original smooth surface). The voltage was set from 0 kV to 3 kV. As a result, the shear force increases by 2.2 N, 1.7 N, 3.1 N, and 2.8 N in smooth, 400 mesh, 800 mesh, and 1200 mesh tin foils respectively. The friction force on the 800 mesh tin foil changes most obviously. Due to the force of the air pressure on the smooth surface, the change of friction force of the tin foil with a lower mesh number is relatively large. Therefore, we chose 800 mesh tin foil as the middle interlayer, which can ensure the most obvious effect of the overall stiffness change of the structure. Then we measured the variable stiffness performance of a unit which was defined as two EA pads sandwiching one interlayer. The stiffness was defined as the pulling force generated by moving a unit distance (Fig. 4(a)). In Fig. 4(b), as the voltage increases, the structural rigidity increases. When no voltage is applied, the structural stiffness is about 1000 N m^{-1}, and when the voltage is 3.5 kV, the stiffness is about 2100 N m^{-1}. The stiffness could be continuously adjusted by voltage. It also shows that the relationship between stiffness and

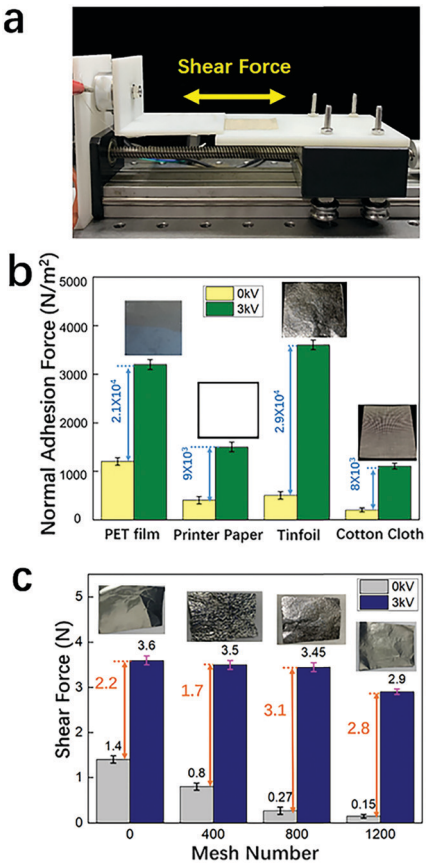

Fig. 3 The shear force of the EA pads. (a) The experimental setup for measuring shear force. (b) The effects of four materials as interlayers. (c) A comparison of the shear force of four types of tin foils with different roughness.

voltage is approximately quadratic before 2 kV. When the voltage exceeds 2.5 kV, the stiffness increase is not significant. The reason for this is that after the voltage has been increased to 2.5 kV, the adsorption force is sufficient to ensure the electrode layers attracting an interlayer firmly with a high friction force, so increasing the voltage will not increase the stiffness as significantly. In Fig. 4(c) a linear relation of the stiffness of the structure was realized. To explore the variable stiffness effect of multiple units stacked together, we measured the performance of structures with a different number of units. In Fig. 4(d) and (e), more units induced a greater initial stiffness of the structure and tuned the stiffness significantly at 3 kV. However, at the same time, the Rate of the Change in Relative Stiffness (RCRS) dropped. The reason for this is due to the fact that with a great initial stiffness, there is a shortened improvement span for stiffness change after power-on.

3. A semi-active vibration absorber based on FEVS artificial muscle

To demonstrate that our FEVS artificial muscle can be readily implemented in engineering applications, we demonstrated a semi-active vibration control method according to the theory of dynamics with variable stiffness.[63,64] The FEVS favors a light

 This journal is © The Royal Society of Chemistry 2021

Published on 27 May 2021. Downloaded on 7/22/2021 12:35:26 PM.

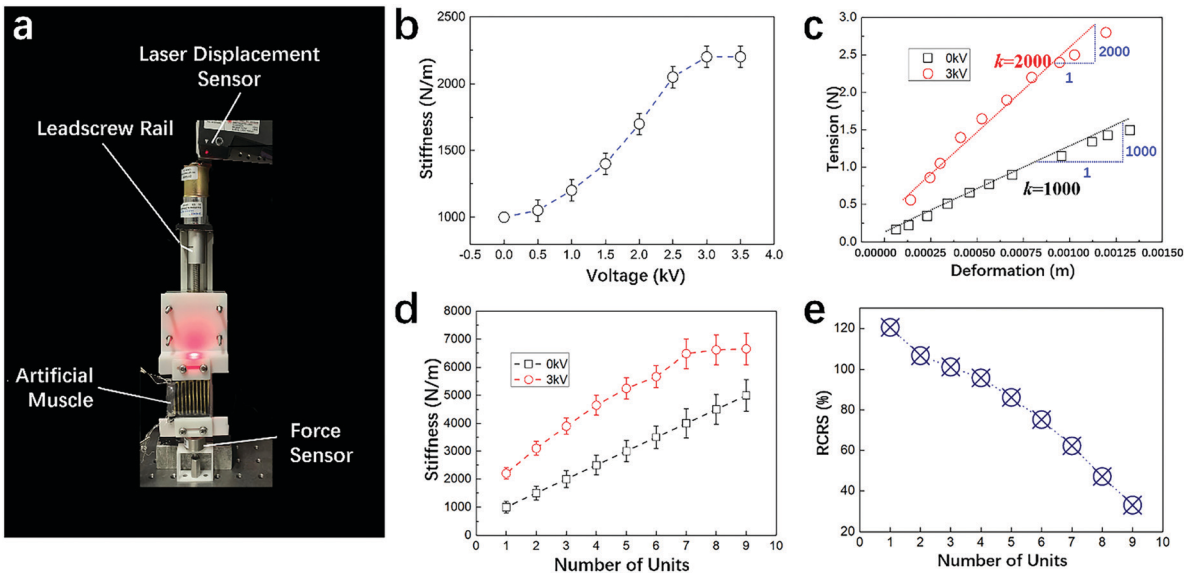

Fig. 4 Variable stiffness measurement of the FEVS artificial muscles. (a) The measurement device. (b) When the voltage changes from 0 kV to 3.5 kV, the effect of the change in the stiffness. The measurement equipment is depicted in the subplot. (c) The data reflects the fact that the tuneable stiffness has a linear character. (d) The variable stiffness effects of structures with different numbers of units. One unit is an EA pad with an interlayer. (e) The number of units, *vs.* the rate of change of relative stiffness (RCRS) with the voltage of 3 kV. The RCRS is defined as the percentage of the changed stiffness value to the initial stiffness value.

weight so that it will not add extra mechanical loading to the structure to be attenuated.

We stacked multiple units of artificial muscles as a vibration absorber to verify its variable stiffness effect. The principle of the absorber is shown in Fig. 5(a). When the voltage is off, there is a gap between the EA pads and the interlayers, and the overall stiffness of the structure is weak. Subject to a voltage, the EA pads attract the interlayers and increased the friction among layers, enhancing the structural rigidity. Fig. 5(b) describes the vertical stiffness test and results of the stacked vibration absorber. With repeatedly placing different masses to compress the absorber, different voltages were applied, and the

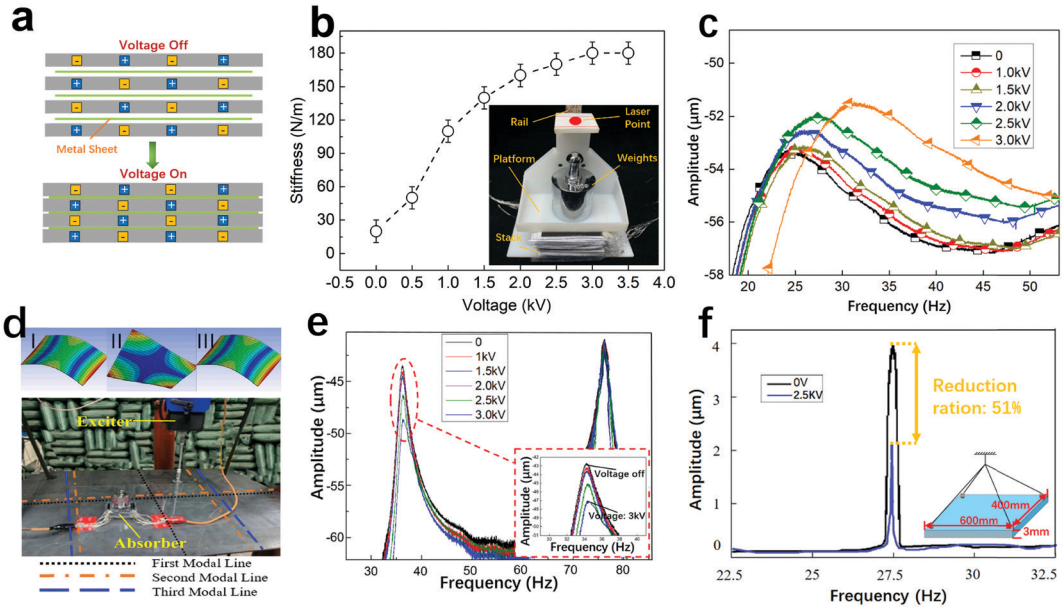

Fig. 5 FEVS artificial muscles as a vibration absorber in semi-active control. (a) The mechanism of the semi-active control absorber by units of FEVS artificial muscles. (b) Vertical variable stiffness measurement of the stack absorber. (c) The performance of absorber in adjusting the natural frequency by voltage. From 0 kV to 3 kV, the NF changes from 24 Hz to 32 Hz. (d) The first three-order modes of the plate to be controlled. The positions of the exciter, the sensors and the actuator were confirmed. (e) The attenuation of steel plate amplitude when different voltages are applied to the absorber. (f) Frequency domain response of a steel plate in amplitude attenuation. When the excitation frequency is 27 Hz, a 2.5 kV voltage was applied to the absorber to tune its natural frequency close to 27 Hz. A vibration reduction effect is realized, and the steel plate amplitude attenuation is 51%.

Published on 27 May 2021. Downloaded on 7/22/2021 12:35:26 PM.

stiffness value under each voltage was obtained. When the voltage was 3.5 kV, the stiffness was about 180 N m^{-1}, increasing by 500% compared with the initial stiffness at voltage off. Under this mechanism, the stacked FEVS artificial muscle is used as a vibration absorber that can adjust its natural frequency by adjusting its stiffness to achieve a function of semi-active control. When the external excitation reaches the natural frequency of the absorber, the absorber resonates, thereby absorbing vibration by reducing the amplitude. We first characterized the performance of the absorber by adjusting its natural frequency.

In Fig. 5(c), the natural frequency of the absorber increased by about 8 Hz, and the experiment details are in the ESI.† A steel plate with a size of 400 mm × 600 mm × 3 mm and four corners suspended is chosen as the target object. The natural frequency is 32 Hz (ESI†). The reason for choosing steel plates as the object of vibration damping is that the plate structure is the most basic mechanical structure and is also the basic components of the unit. Through the simulation analysis of the suspension steel plate, its first three-order modes were obtained (Fig. 5(d)). This helps us to determine the distribution of the absorber and the exciter, avoiding the node line. The physical model of the vibration attenuation system could be simplified to a single degree of freedom system, as shown in Fig. 6(a). The mass of the main system is m_1, the stiffness is k_1, and the mass of the semi-active vibration absorber is m_2, the stiffness is k_2, and the damping is c. Suppose the motivation is $P_1e^{i\omega t}$, which acts on the main system. Suppose the displacement of the vibration system is as eqn (3). And x_1 and x_2 are the displacement of the main system and the vibration absorber, and $\bar{B}_1$ and $\bar{B}_2$ are the complex amplitude.

$$\begin{bmatrix} x_1 \\ x_2 \end{bmatrix} = \begin{bmatrix} \bar{B}_1 \\ \bar{B}_2 \end{bmatrix} e^{i\omega t} \tag{3}$$

A mathematical model of the vibration control system is established in eqn (4).

$$\begin{bmatrix} m_1 & 0 \\ 0 & m_2 \end{bmatrix} \begin{bmatrix} \ddot{x}_1 \\ \ddot{x}_2 \end{bmatrix} + \begin{bmatrix} c & -c \\ -c & c \end{bmatrix} \begin{bmatrix} \dot{x}_1 \\ \dot{x}_2 \end{bmatrix} + \begin{bmatrix} k_1 + k_2 & -k_2 \\ -k_2 & k_2 \end{bmatrix} \begin{bmatrix} x_1 \\ x_2 \end{bmatrix} = \begin{bmatrix} P_1 e^{i\omega t} \\ 0 \end{bmatrix} \tag{4}$$

Incorporating eqn (3) into eqn (4), we have

$$\begin{bmatrix} \bar{B}_1 \\ \bar{B}_2 \end{bmatrix} = \begin{bmatrix} k_1 + k_2 - m_1\omega^2 + ic\omega & -(k_2 + ic\omega) \\ -(k_2 + ic\omega) & k_2 - m_2\omega^2 + ic\omega \end{bmatrix}^{-1} \begin{bmatrix} P_1 \\ 0 \end{bmatrix} = \frac{P_1}{\Delta(\omega)} \begin{bmatrix} k_2 - m_2\omega^2 + ic\omega \\ k_2 + ic\omega \end{bmatrix} \tag{5}$$

$\Delta(\omega)$ is the characteristic polynomial of the system, and its expression is as eqn (6).

$$\begin{aligned} \Delta(\omega) &= (k_1 + k_2 - m_1\omega^2 + ic\omega)(k_2 - m_2\omega^2 + ic\omega) - (k_2 + ic\omega)^2 \\ &= (k_1 - m_1\omega^2)(k_2 - m_2\omega^2) - k_2m_2\omega^2 \\ &\quad + ic\omega(k_1 - m_1\omega^2 - m_2\omega^2) \end{aligned} \tag{6}$$

Therefore, the complex amplitude of the main system is obtained.

$$\bar{B}_1 = \frac{P_1(k_2 - m_2\omega^2 + ic\omega)}{(k_1 - m_1\omega^2)(k_2 - m_2\omega^2) - k_2m_2\omega^2 + ic\omega(k_1 - m_1\omega^2 - m_2\omega^2)} \tag{7}$$

Supposing $\delta_{st} = \frac{P_1}{k_1}$, and the natural frequency of the main system is $\omega_0 = \sqrt{\frac{k_1}{m_1}}$, the natural frequency of the vibration absorber is $\omega_a = \sqrt{\frac{k_2}{m_2}}$. The mass ratio of the shock absorber to the main system is $\mu = \frac{m_2}{m_1}$. And $\alpha = \frac{\omega_a}{\omega_0}$, $\lambda = \frac{\omega}{\omega_0}$, $\xi = \frac{c}{2m_2\omega_0}$. Modulo $\bar{B}_1$. The amplitude of the main system is.

$$B_1 = \delta_{st}\sqrt{\frac{(\lambda^2 - \alpha^2)^2 + (2\xi\lambda)^2}{[\mu\lambda^2\alpha^2 - (\lambda^2 - 1)(\lambda^2 - \alpha^2)]^2 + (2\xi\lambda)^2(\lambda^2 - 1 + \mu\lambda^2)^2}} \tag{8}$$

k_2 is the stiffness of the vibration absorber and ω_a is the natural frequency of the vibration absorber. They are regulated by voltage. Therefore, the natural frequency ratio α and λ in eqn (8) will change in real time according to the needs of the system. We set, $c \approx 2.8$ N s m^{-1} and $\mu = 0.025$ according to the

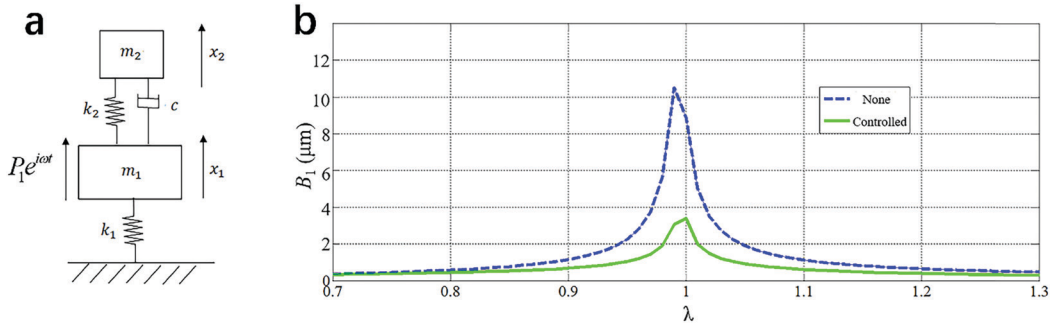

Fig. 6 (a) Physical model of semi-active vibration attenuation system. (b) Simulation results of vibration absorption when the external excitation frequency is equal to the natural frequency of the main system.

 This journal is © The Royal Society of Chemistry 2021

Published on 27 May 2021. Downloaded on 7/22/2021 12:35:26 PM.

material properties. With the help of MATLAB, we conducted a simulation test on the vibration attenuation system, and the experimental results are shown in Fig. 6(b). When the external excitation frequency was equal to the main system, the amplitude attenuation effect of the system before and after the control was the most obvious, reaching 7 μm.

Then we performed experiments and measured the amplitude of the steel plate after applying different voltages to the absorber. When the voltage was 3.5 kV, the natural frequency of the absorber was 31 Hz, which was close to the natural frequency of the steel plate, and the amplitude of the steel plate attenuation, 4.5 μm, was similar to the result of the simulation (Fig. 5(e)). The experimental result was smaller than the simulation result is because the natural frequency of the vibration absorber was not completely equal to the natural frequency of the main system. Meanwhile, the damping of the vibration absorber after the stiffness increased would be smaller, which also affected the vibration absorption effect. Then we measured the vibration damping effect at frequencies away from natural frequency. As shown in Fig. 5(f), we fixed the frequency of 27 Hz to excite the steel plate and applied a voltage of 2.5 kV to the absorber. In Fig. 5(c), the natural frequency of the absorber at 2.5 kV is 27 Hz. There is an amplitude attenuation by about 51% utilizing the FEVS artificial muscle absorber.

4. Comparing the FEVS artificial muscle with others

To evaluate the variable stiffness performance, we compared with other sandwich-type artificial muscles. One is the electrostatic layer jamming laminates (ELJ) in the layer structure, and the other is the pneumatic jamming muscle (Fig. 7(a)).[65] The process of the manufacturing was exactly followed according to the related literature and the performances were identical with the reports.[40,65]

ELJ is composed of conductive layers with opposite polarities and interlayers. All materials corresponded to are the same as the FEVS artificial muscle.[40,42,66] The principle of ELJ is as follows: adjacent conductive layers are applied with opposite voltages, and an electric field through the interlayer will be generated between them, which makes them attract each other. The electrical field compresses the interlayer, increases the frictional force, and therefore changes the stiffness of the whole structure. The pneumatic jamming muscle consists of two cover layers and a fibre layer in the middle. The sides of the structure are sealed, and there is an air outlet, which is connected to the outside space through a pipe. The cover layer material is silicone rubber, and the fibre layer material is a plurality of polyester fibre filaments with a diameter of 0.5 mm. We manufactured the above two artificial muscles, the overall dimensions are both 40 mm × 40 mm, which are the same as the FEVS artificial muscle. ELJ was applied with different voltages with a selected thickness of 400 μm of the interlayer. Using the same method in Fig. 4(a), the effect of stiffness change is shown in Fig. 7(b). Under the same thickness and applied voltage, the performance of FEVS artificial muscle was more significant. In Fig. 7(c), regarding the different thickness of the intermediate layer, the rate of change of relative stiffness of FEVS artificial muscle hardly changed. However, for ELJ, the great thickness of the interlayer reduces the rate change. The reason is that the FEVS artificial muscle uses fringe electric field polarization to the

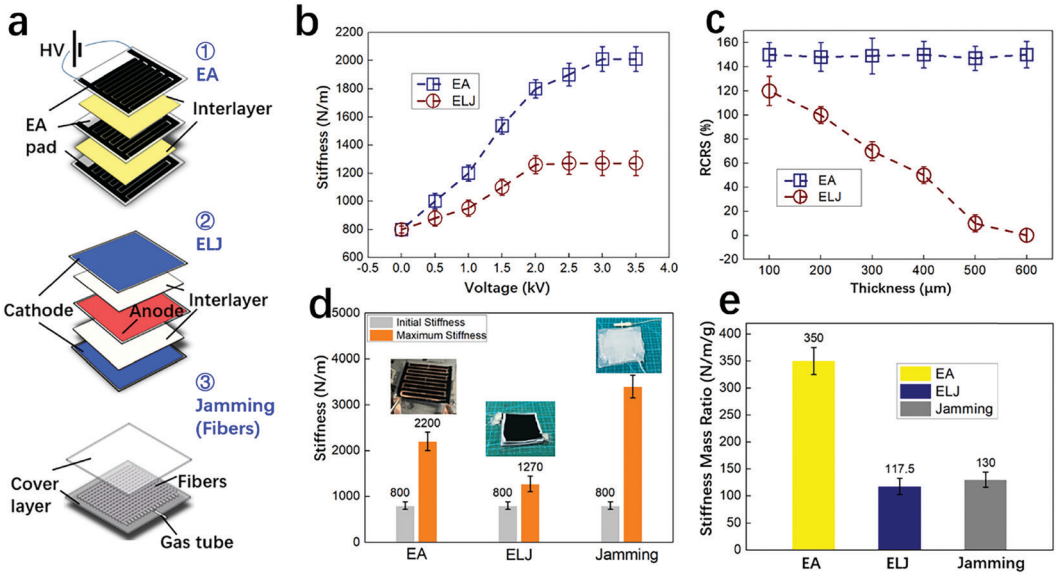

Fig. 7 Comparison of three variable stiffness artificial muscles. (a) Schematic diagrams of FEVS artificial muscle, ELJ and pneumatic jamming structure. (b) The comparison of variable stiffness between FEVS artificial muscle and ELJ. (c) Different performances of variable stiffness when the thickness of the interlayer changes between FEVS artificial muscle and ELJ. (d) The maximum and minimum stiffness of three artificial muscles. (e) The stiffness mass ratio of three artificial muscles, which is the ratio of the maximum stiffness change to its weight. The masses of FEVS artificial muscle, ELJ and jamming structure are 4 g, 4 g and 20 g, respectively.

Published on 27 May 2021. Downloaded on 7/22/2021 12:35:26 PM.

surface of the interlayer to achieve attraction, so the magnitude of the force does not depend on the thickness of the interlayer. But for ELJ, it mainly relies on the mutual attraction between the plates. When the thickness of the interlayer increases, the distance between the plates becomes longer, the electric field strength will be weakened, and the pressure will also be reduced. Therefore, compared with ELJ, the variable stiffness effect in the FEVS artificial muscle is not affected by the thickness of the interlayer. Because the pneumatic jamming structure is not dependent on an electrical mechanism, which is why we did not compare it with the FEVS artificial muscle and ELJ in Fig. 7(b) and (c). We put the three variable stiffness structures together for comparison. The results are summarized in Fig. 7(d). The variable stiffness effect of the pneumatic jamming structure is the most obvious. Soft robots that require a variable stiffness component, its compliance and light weight shall be sacrificed minimally. Thus, we define the stiffness to weight ratio to highlight the advantage of the stiffness change per unit weight, as in Fig. 7(e).

The value of the pneumatic jamming structure is relatively small, while the FEVS artificial muscle has the highest ratio. Compared with the other two lightweight variable stiffness structures, FEVS is more likely to derive a benefit for the design of lightweight soft robotics with the application of variable stiffness.

5. Conclusions

We have proposed a variable stiffness artificial muscle that could be used for semi-active vibration control. This artificial muscle is based on the fringe electric field adhesion principle and fabricated by 3D printing (DIW). The anti-stretching and anti-pressing stiffness of this artificial muscle increased 100% and 500% respectively at an electric field of 3 kV mm^{-1}. The vibration absorber based on the stacked FEVS could attenuate the vibration amplitude of the steel plate by 51%. In addition, FEVS is lightweight, flexible and its stiffness is irrelevant to the thickness of the interlayer. Thus, it will be beneficial to the variable stiffness technology of lightweight soft robots.

6. Materials and methods

Materials and characterization

The 3D printer was self-built with a 3D printing system composed of a computer-controlled three-axis motion platform. The printing paths were decided by G-code commands, which were supported by commercial software (CuraEngine) based on the designed 3D model (SolidWorks). The silicone rubber (186 series) was purchased from Dow Corning Co., Ltd of US. Carbon nanotube (TNSM3 type) was purchased from Chengdu Organic Chemicals Co., Ltd of the Chinese Academy of Science. Polydimethylsiloxane composite materials (184) were purchased from Dow Corning Co., Ltd of US. Polyester film (100 μm thick) was purchased from Shenzhen White Mist Film Co., Ltd. Printing paper (100 μm thick) was purchased from Hangzhou Deli Co., Ltd. Tin foil (100 μm thick) was purchased from Dongguan Juyou Co., Ltd. Cotton cloth (100 μm thick) was purchased from Huzhou Wanyue Co., Ltd. The fibre (diameter of 0.128 mm) used in the pneumatic jamming structure was purchased from Shanghai Mermaid Fishing Tackle Co., Ltd.

Force measurement

Fig. 2(b) and 3(a) show the measuring devices of the normal force and shear force respectively. The principle is as follows: one end of the force sensor is fixed on the desktop, and the other end is connected with the electrode layer sample, the adsorbed object is fixed on the part opposite to the electrode layer, and the part is controlled to move slowly and uniformly on the guide rail to reach the absorbed object and until the electrode layer sample is attached. The criterion for judging the attachment is the moment when the signal from the force sensor is collected to the pressure, the programmed feedback controls the moving part to be powered off, and the moving part stops moving to ensure that it is in the attached state. The sample is applied with voltage (3 kV), and the moving parts are reversely controlled to separate the absorbed object from the electrode layer. Since the EA pad has an absorption force on the absorbed object, the force sensor can collect the force signals when the two separate recordings the electrostatic attraction force.

Vibration tests

We applied different voltages (0–3 kV) to the absorber and used an exciter (the model K2007E01 produced by MTS Sensors is an intelligent vibration exciter with an integrated power amplifier) to excite it by frequency sweeping (0–100 Hz, 0.5 N), then we got the character by adjusting the natural frequency of the absorber in different voltages with a laser displacement sensor (LK-G80 from Keyence Co., Ltd). Fig. 5(d) shows the principle of the vibration control test. We used an exciter with diverse frequencies to excite the steel plate and applied different voltages to the absorber. With the help of acceleration sensors (SN 208 from Kistler Co., Ltd), the amplitudes were measured and the effect of semi-active control (capability of variable stiffness) was verified. The signal generator (DG4062, Puyuan Co., Ltd) generated various voltage signals such as sine wave, square wave and DC signal, to the amplifier (20/20 Hs, Trek Co., Ltd) which can amplify the input voltage signal by 2000 times for actuation. The finite element modeling shown in Fig. 5(d) was in the commercial software package *ANSYS* 15.0, from Swanson Analysis Systems, Inc.

Author contributions

C. L., B. L., K. Z. and H. C. conceived and designed the experiment. C. L. and Z. L. conducted the experiments and recorded data. The manuscript was written through contributions of all authors. All authors have given approval to the final version of the manuscript.

Conflicts of interest

There are no conflicts to declare.

 This journal is © The Royal Society of Chemistry 2021

Published on 27 May 2021. Downloaded on 7/22/2021 12:35:26 PM.

Acknowledgements

This work was supported in part by the National Key R&D Program of China under Grant No. 2019YFB1311600, the National Natural Science Foundation of China under Grant No. 52075411, Shaanxi Key R&D Program (2020ZDLGY06-11), Shenzhen Fundamental Research Project (NO. JCYJ20200109115639654), the EPSRC in framework of the NCNR (National Centre for Nuclear Robotics) project (EP/R02572X/1) and NCNR flexifund (1473135), and the China Scholarship Council (CSC).

References

1 J. Wang, D. Gao and P. S. Lee, *Adv. Mater.*, 2020, 2003088.
2 Q. He, Z. Wang, Y. Wang, Z. Song and S. Cai, *ACS Appl. Mater. Interfaces*, 2020, **12**, 35464–35474.
3 A. J. Veale, K. Staman and H. van der Kooij, *Soft Robot.*, 2020, **5**, 1–5.
4 J. Park, J. Choi, S. J. Kim, K.-H. Seo and J. Kim, *IEEE Robot. Autom. Lett.*, 2020, **5**, 3799–3805.
5 S. M. Mirvakili, D. Sim, I. W. Hunter and R. Langer, *Sci. Robot.*, 2020, **5**, 41.
6 Q. Guan, J. Sun, Y. Liu, N. M. Wereley and J. Leng, *Soft Robot.*, 2020, **7**, 597–614.
7 L. Sun, Y. Yu, Z. Chen, F. Bian, F. Ye, L. Sun and Y. Zhao, *Chem. Soc. Rev.*, 2020, **49**, 4043–4069.
8 L. Shang, Y. Yu, Y. Liu, Z. Chen, T. Kong and Y. Zhao, *ACS Nano*, 2019, **13**, 2749–2772.
9 Z. C. Jiang, Y. Y. Xiao, X. Tong and Y. Zhao, *Angew. Chem., Int. Ed.*, 2019, **58**, 5332–5337.
10 J. A.-C. Liu, J. H. Gillen, S. R. Mishra, B. A. Evans and J. B. Tracy, *Sci. Adv.*, 2019, **5**, eaaw2897.
11 P. H. Nguyen and W. Zhang, *Sci. Rep.*, 2020, **10**, 1–13.
12 S. R. Shin, B. Migliori, B. Miccoli, Y. C. Li, P. Mostafalu, J. Seo, S. Mandla, A. Enrico, S. Antona and R. Sabarish, *Adv. Mater.*, 2018, **30**, 1704189.
13 Z. Jiao, C. Zhang, W. Wang, M. Pan, H. Yang and J. Zou, *Adv. Sci.*, 2019, **6**, 1901371.
14 M. Mahato, R. Tabassian, S. Oh, S. Nam, W.-J. Hwang and I.-K. Oh, *Nat. Commun.*, 2020, **11**, 1–15.
15 N. T. Jafferis, E. F. Helbling, M. Karpelson and R. J. Wood, *Nature*, 2019, **570**, 491–495.
16 H. Godaba, A. Sajad, N. Patel, K. Althoefer and K. Zhang, *IROS*, 2020, 8716–8721.
17 J. Zhou, Y. Chen, Y. Hu, Z. Wang, Y. Li, G. Gu and Y. Liu, *Soft Robot.*, 2020, **7**, 743–757.
18 X.-Y. Guo, W.-B. Li, Q.-H. Gao, H. Yan, Y.-Q. Fei and W.-M. Zhang, *Smart Mater. Struct.*, 2020, **29**, 035033.
19 I. Must, E. Sinibaldi and B. Mazzolai, *Nat. Commun.*, 2019, **10**, 1–8.
20 W.-B. Li, W.-M. Zhang, H.-X. Zou, Z.-K. Peng and G. Meng, *Smart Mater. Struct.*, 2017, **26**, 085033.
21 M. Luo, L. Liu, C. Liu, B. Li, C. Cao, X. Gao and D. Li, *IEEE Trans. Ind. Electron.*, 2020, 3013544.
22 S. T. Chang, A. B. Uçar, G. R. Swindlehurst, R. O. Bradley IV, F. J. Renk and O. D. Velev, *Adv. Mater.*, 2009, **21**, 2803–2807.
23 I. K. Kuder, A. F. Arrieta, W. E. Raither and P. Ermanni, *Prog. Aerosp. Sci.*, 2013, **63**, 33–55.
24 B. Pokroy, A. K. Epstein, M. C. Persson-Gulda and J. Aizenberg, *Adv. Mater.*, 2009, **21**, 463–469.
25 F.-Y. Xu, F.-Y. Jiang, Q.-S. Jiang and Y.-X. Lu, *IEEE Access*, 2020, **8**, 26356–26371.
26 M. R. A. Bhatti, E. Bilotti, H. Zhang, S. Varghese, R. C. Verpaalen, A. P. Schenning, C. W. Bastiaansen and T. Peijs, *ACS Appl. Mater. Interfaces*, 2020, **12**, 33210–33218.
27 M. A. Robertson and J. Paik, *Sci. Robot.*, 2017, **2**(9), eaan6357.
28 V. K. Venkiteswaran, R. Hu and H. Su, *ROBIO*, 2018, 1–7.
29 A. R. Deshpande, Z. T. H. Tse and H. Ren, *ICRA*, 2017, 417–421.
30 S. Li, D. M. Vogt, D. Rus and R. J. Wood, *Proc. Natl. Acad. Sci. U. S. A.*, 2017, **114**, 13132–13137.
31 Y. S. Narang, J. J. Vlassak and R. D. Howe, *Adv. Funct. Mater.*, 2018, **28**, 1707136.
32 Y. Li, T. Ren, Y. Chen and M. Z. Chen, *ICRA*, 2020, 5869–5875.
33 J. Paik, *Soft Components for Soft Robots*, Springer, Berlin Heidelberg, 2015, pp. 272–281.
34 D. Nalini, A. Nandakumar, A. Sampath and K. Dhanalakshmi, *I2CT*, 2019, 1–5.
35 J. Shintake, B. Schubert, S. Rosset, H. Shea and D. Floreano, *IROS*, 2015, 1097–1102.
36 M. A. McEvoy and N. Correll, *Science*, 2015, 347.
37 T. Helps, M. Taghavi, S. Wang and J. Rossiter, *Soft Robot.*, 2020, **7**, 386–395.
38 T. L. Buckner, M. C. Yuen, S. Y. Kim and R. Kramer-Bottiglio, *Adv. Funct. Mater.*, 2019, **29**, 1903368.
39 D. Zappetti, S. H. Jeong, J. Shintake and D. Floreano, *Soft Robot.*, 2020, **7**, 362–369.
40 T. Wang, J. Zhang, Y. Li, J. Hong and M. Y. Wang, *IEEE/ASME Trans. Mechatron.*, 2019, **24**, 424–433.
41 A. Zahedi, B. Zhang, A. Yi and D. Zhang, Soft Robot., 2020.
42 R. Hinchet and H. Shea, *Adv. Mater. Technol.*, 2020, **5**, 1900895.
43 Q. Wang, X. Dong, L. Li and J. Ou, *Smart Mater. Struct.*, 2017, **26**, 105028.
44 H. Imamura, K. Kadooka and M. Taya, *Soft Matter*, 2017, **13**, 3440–3448.
45 E. Piskarev, J. Shintake, V. Ramachandran, N. Baugh, M. D. Dickey and D. Floreano, *Adv. Intell. Syst.*, 2020, **2**, 2000069.
46 J. Guo, J. Leng and J. Rossiter, *IEEE Trans. Robot.*, 2019, **36**, 313–327.
47 M. Duduta, R. J. Wood and D. R. Clarke, *EAPAD*, 2016, **9798**, 97981D.
48 J. Cao, L. Qin, J. Liu, Q. Ren, C. C. Foo, H. Wang, H. P. Lee and J. Zhu, *Extreme Mech. Lett.*, 2018, **21**, 9–16.
49 M. Graule, P. Chirarattananon, S. Fuller, N. Jafferis, K. Ma, M. Spenko, R. Kornbluh and R. Wood, *Science*, 2016, **352**, 978–982.
50 L. Pan, P. Cai, L. Mei, Y. Cheng, Y. Zeng, M. Wang, T. Wang, Y. Jiang, B. Ji and D. Li, *Adv. Mater.*, 2020, **32**, 2003723.
51 S. D. de Rivaz, B. Goldberg, N. Doshi, K. Jayaram, J. Zhou and R. J. Wood, *Sci. Robot.*, 2018, **3**, eaau3038.
52 J. Guo, K. Elgeneidy, C. Xiang, N. Lohse, L. Justham and J. Rossiter, *Smart Mater. Struct.*, 2018, **27**, 05506.
53 J. Shintake, S. Rosset, B. Schubert, D. Floreano and H. Shea, *Adv. Mater.*, 2016, **28**, 231–238.

54 A. Chortos, E. Hajiesmaili, J. Morales, D. R. Clarke and J. A. Lewis, *Adv. Funct. Mater.*, 2020, **30**, 1907375.
55 Y. Okuno, H. Shigemune, Y. Kuwajima and S. Maeda, *Adv. Mater. Technol.*, 2019, **4**, 1800304.
56 S. Park, D. S. Drew, S. Follmer and J. Rivas-Davila, *IEEE Robot. Autom. Lett.*, 2020, **5**, 4485–4492.
57 J. Mao, L. Qin, Y. Wang, J. Liu and L. Xue, *IEEE International Conference on Mechatronics and Automation*, 2014, 987–992.
58 K. H. Koh, R. K. Chetty and S. Ponnambalam, *IEEE International Conference on Robotics and Biomimetics*, 2011, 2031–2036.
59 D. A. Jones and J. M. Round, *Skeletal muscle in health and disease: a textbook of muscle physiology*, Manchester University Press, 1990.
60 J. C. Tai Y, F. Xiaoli and W. Tinghuai, *Excitation-contraction coupling of rhabdoid muscle cells*, People's Medical Publishing House, Physiology, 2013, vol. 2.
61 G. Hwang, J. Park, D. S. D. Cortes, K. Hyeon and K.-U. Kyung, *IEEE Trans. Ind. Electron.*, 2021, DOI: 10.1109/TIE.2021.3053887.
62 A. S. Chen and S. Bergbreiter, *Smart Mater. Struct.*, 2017, **26**, 025028.
63 W. Hu, Y. Gao, X. Sun, Y. Yang and B. Yang, *J. Vib. Control*, 2019, **25**, 2819–2833.
64 S. Sarkar and A. Chakraborty, *J. Sound Vib.*, 2019, **457**, 15–36.
65 L. Liu, J. Zhang, Y. Cai, B. Li, G. Liu and P. Li, *Smart Mater. Struct.*, 2020, **9**, 125013.
66 D. Rus and M. T. Tolley, *Nature*, 2015, **521**, 467–475.

Published on 27 May 2021. Downloaded on 7/22/2021 12:35:26 PM.

 This journal is © The Royal Society of Chemistry 2021